Research Square

Preprints are preliminary reports that have not undergone peer review.
They should not be considered conclusive, used to inform clinical practice,
or referenced by the media as validated information.

Electrically Controlled Spatial Light Modulator for Ultrawideband Hyperspectral Terahertz Single-Pixel Imaging

Yiwen Sun

775319806@qq.com

Key Laboratory of Optoelectronic Devices and Systems of Ministry of Education and Guangdong Province, College of Physics and Optoelectronics Engineering,

Xudong Liu

Department of Biomedical Engineering, School of Medicine, Shenzhen University

Wenjing Ma

Shenzhen University

Chuanfu Sun

Department of Biomedical Engineering, School of Medicine, Shenzhen University

Emma Pickwell-MacPherson

University of Warwick https://orcid.org/0000-0001-6062-5959

Yu Liao

Department of Biomedical Engineering, School of Medicine,

Xiaoyu Weng

Shenzhen University https://orcid.org/0000-0001-9654-3517

Junle Qu

Shenzhen University https://orcid.org/0000-0001-7833-4711

Songlin Zhuang

University of Shanghai for Science and Technology

Chenyu Wang

Department of Biomedical Engineering, School of Medicine,

Article

Keywords:

Posted Date: March 4th, 2026

DOI: https://doi.org/10.21203/rs.3.rs-9001286/v1

License: This work is licensed under a Creative Commons Attribution 4.0 International License.
Read Full License

Additional Declarations: There is no conflict of interest

Electrically Controlled Spatial Light Modulator for Ultrawideband Hyperspectral Terahertz Single-Pixel Imaging

Xudong Liu[1], Wenjing Ma[2], Chenyu Wang[3], Chuanfu Sun[3], Yu Liao[3], Emma Pickwell-MacPherson[4], Xiaoyu Weng[1¶], Junle Qu[1#], Songlin Zhuang[5] & Yiwen Sun[1*]

[1]Key Laboratory of Optoelectronic Devices and Systems of Ministry of Education and Guangdong Province, College of Physics and Optoelectronics Engineering, Shenzhen University, Shenzhen, 518060, China

[2]National Engineering Laboratory for Big Data System Computing Technology, Shenzhen University, Shenzhen 518060, China

[3]Department of Biomedical Engineering, School of Medicine, Shenzhen University, Shenzhen 518060, China

[4]Department of Physics, University of Warwick, Coventry CV4 7AL, United Kingdom

[5]School of Optical-Electrical and Computer Engineering, University of Shanghai for Science and Technology, Shanghai, China

¶xiaoyu@szu.edu.cn, #jlqu@szu.edu.cn, *ywsun@szu.edu.cn

Abstract:

Terahertz (THz) spectroscopic imaging offers significant potential due to its non-destructive penetration and spectral fingerprinting capabilities. However, existing systems face limitations such as high cost, slow acquisition speed, and limited bandwidth, particularly due to the reliance on non-electrical modulators or expensive detector arrays. Here, we present the first electrically controlled spatial light modulator (SLM) for ultrawideband terahertz hyperspectral single-pixel imaging. Our device, based on a non-resonant GaAs Schottky microslit array, provides direct electrical control over both amplitude and phase modulation across a bandwidth of 0.2-1.4 THz. This design offers a compact, low-cost, and highly integrable solution. Utilizing a 100-pixel array operating at ~3.4 kHz, we demonstrated hyperspectral imaging and depth-resolved 3D reconstruction using a single photoconductive detector in both transmission and reflection modes, achieving a frame acquisition time of approximately 9 seconds. This integration of electrically tunable modulation with ultrabroad bandwidth establishes a new paradigm for terahertz imaging, paving the way for applications in biomedical diagnostics, chemical identification, multilayer inspection, and security screening.

Introduction

In recent decades, terahertz (THz) imaging technologies have made remarkable progress, finding novel applications across various fields, including biomedical imaging [1], quality assurance in pharmaceuticals [2], agricultural products [3], and cultural heritage preservation [4]. This progress can largely be attributed to the low energy of terahertz photons, their ultrawideband spectroscopic information, and their ability to penetrate many non-conductive materials.

Despite its tremendous potential, the practical application of terahertz imaging has

been hampered by significant challenges, including slow image acquisition, large system footprints, and high costs. Current terahertz detector arrays, such as those based on field-effect transistors [5] or microbolometers [6], often lack the capability to capture time-resolved or frequency-resolved image data and phase information. Additionally, their high-cost limits widespread adoption. Most systems rely on raster scanning, leading to slow acquisition speeds and cumbersome setups.

Techniques involving electro-optic (EO) effects in nonlinear crystals can convert THz signals to the near-infrared for detection with optical cameras [6]. However, these systems typically rely on large, expensive high-energy lasers, and the imaging area is often limited. Recent advances in terahertz focal-plane arrays (THz-FPAs) enable direct acquisition of spatial, temporal, and spectral information [7], but they usually require femtosecond lasers, restricting their use to coherent systems like THz-TDS. High-power continuous-wave terahertz sources are often preferred for many practical applications.

An alternative solution for achieving high-speed and affordable terahertz imaging involves integrating spatial light modulators (SLMs) with single-pixel imaging algorithms. This approach can significantly reduce system complexity and cost while maintaining high imaging speeds by leveraging dynamic control of THz wavefronts. However, existing wideband SLMs, including mechanical [8,9] and optical [10,11] designs, are constrained by slow speeds or reliance on large, high-power lasers. Critically, electrical THz-SLMs capable of providing simultaneous amplitude and phase information over a large spectral bandwidth are still lacking.

The integration of such capabilities into a single-pixel imaging system would enable a host of new applications, including revealing unique spectral characteristics of samples and offering 3D imaging reconstruction. To address this challenge, we introduce the first ultrawideband electrical THz-SLM, capable of simultaneously providing amplitude and phase information for hyperspectral imaging. Our SLM, consisting of a 100-pixel array, was integrated into a THz-TDS system, achieving ultrawideband single-pixel imaging with a bandwidth exceeding 1 THz. The system successfully reconstructed 3D images from terahertz temporal signals in both transmission and reflection modes. Furthermore, our ultrawideband SLM can be easily integrated with both THz-TDS and continuous-wave terahertz systems. This innovation could significantly advance cost-effective, high-speed imaging and inspection

technologies by leveraging the unique spectral properties of terahertz radiation, opening new applications in biomedical imaging, security screening, agriculture, and quality assurance.

Results

Concept and design of the ultrawideband THz-SLM

Figure 1 illustrates the schematic and operational principles of our terahertz single-pixel imaging system, which integrates an ultrawideband THz-SLM with a THz-TDS system. The sample under study comprises three distinct materials, each with different transmission spectra in the terahertz band—denoted by their central frequencies f_1, f_2, and f_3, respectively. The transmitted terahertz beam is spatially encoded by the SLM and collected by a single detector. The sample image is then reconstructed by sequentially adjusting the SLM patters and applying a compressive sensing (CS) algorithm to decode the spatial information.

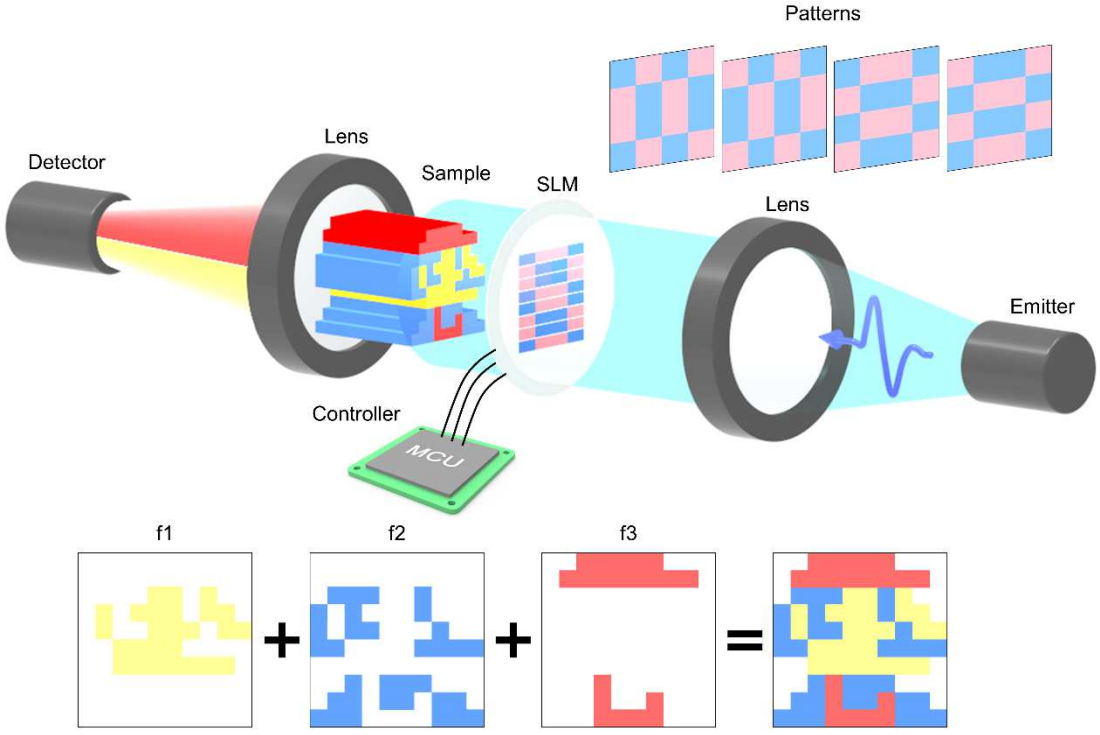


Figure 1. Schematic of the ultrawideband THz-SLM imaging system. The SLM is positioned in front of the target object to project a sequence of structured illumination patterns. A transmitted terahertz beam is spatially modulated by the SLM, transmits through the sample, and is subsequently collected by a single-pixel detector. The patterning sequence of the SLM is governed by a microcontroller unit (MCU). The sample—represented here by a pixelated "Mario" graphic—comprises materials exhibiting three distinct terahertz spectral colors, denoted as f_1, f_2 , and f_3.

Device fabrication and characterization

Figure 2 illustrates the design and fabrication process of our electrically controlled

terahertz spatial light modulator (THz-SLM). The device consists of a 10×10 pixel array fabricated on a lightly n-doped GaAs substrate. Each pixel incorporates a subwavelength gold microslit array forming a Schottky contact with the substrate, with a periodicity of p = 8 μm and a gap width of g = 2 μm. Ohmic contacts were realized by depositing gold stripes between the microslits, spaced 100 μm apart from the Schottky contacts. Each pixel is independently addressed via a custom microcontroller unit (MCU) applying a reverse bias of 5 V between the Schottky and Ohmic contacts. The incident terahertz wave, polarized perpendicularly to the microslits, exhibits high transmission modulated by free carriers within the microslit gaps. This design leverages a non-resonant field enhancement effect, confining the terahertz wave within the gaps and significantly improving modulation performance.

Application of a 5 V reverse bias depletes free carriers, forming a depletion region corresponding to the "ON" state (element "1"). In the absence of bias (0 V), the pixel attains high attenuation, representing the "OFF" state (element "0"). A photograph of the fabricated SLM is shown in Figure 2c, where each pixel (3×3 mm²) is wire-bonded to a printed circuit board (PCB), forming a total active area of 34×34 mm². Detailed fabrication procedures are provided in the Supplementary Information.

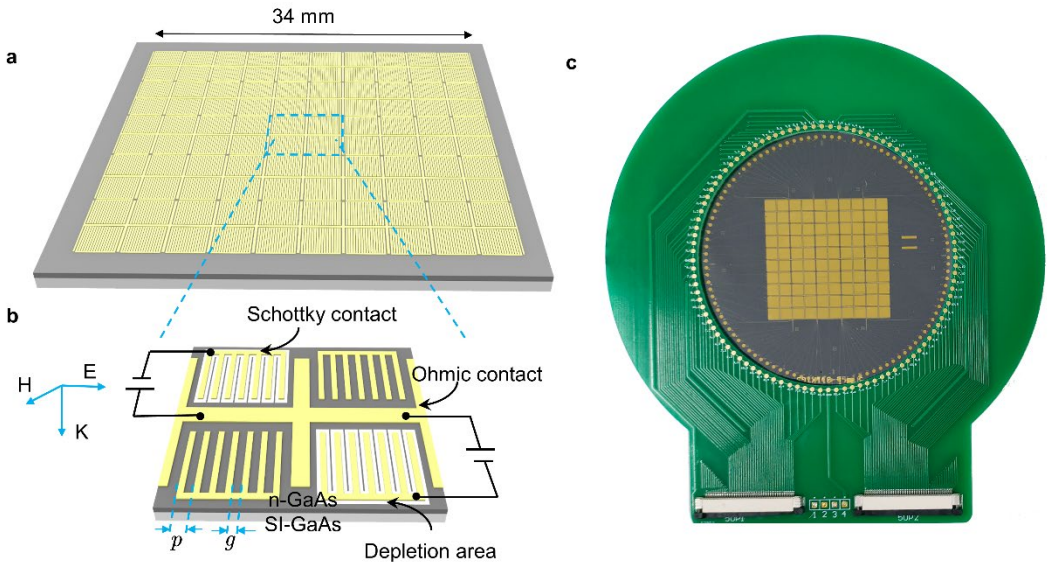


Figure 2. Schematic of the wideband electrical THz-SLM. a. The THz-SLM consists of a 10×10pixel array. Each pixel measures 3×3 mm², resulting in a total active area of 34 mm×34 mm². **b.** The device is fabricated on a lightly *n*-doped GaAs layer (*n*-GaAs) epitaxially grown on a semi-insulating GaAs (SI-GaAs) substrate. Each pixel is independently controlled via a reverse bias applied between the Schottky and Ohmic contacts, generating a tunable carrier-depletion region (white area). Key geometric parameters include the microslit period (p) and gap width (g). The incident terahertz electric field is polarized perpendicular to the microslit direction. **c.** Photograph of the fabricated THz-SLM, highlighting its electrical connections to the PCB.

Characterization of pixel performance

We evaluated the SLM performance using a terahertz time-domain spectroscopy (TDS) system in a single-pixel imaging configuration (Figure 3a). Initial raster scanning of individual pixels revealed a clear increase in transmitted terahertz amplitude as the applied voltage switched from 0 V to 5 V (Figure 3b). The modulation depth (MD) was calculated as:

$$MD=(1-E_V^2/E_{max}^2)\times 100\% \quad (1)$$

where E_V is the frequency-dependent amplitude of the terahertz signal at bias voltage V, and E_{max} is the maximum amplitude at 5 V. As shown in Figure 3c, the MD exceeds 20% over the 0.2-0.6 THz range, demonstrating broadband modulation across 0.2-1.4 THz. This frequency-dependent behavior aligns with the Drude-model response of free carriers in the n-GaAs layer [14].

The modulation speed, governed by carrier mobility in n-GaAs and the RC time constant, was characterized by applying a square-wave AC bias (0-5 V). The rise time was measured as 290 μs, corresponding to a modulation bandwidth of ~3.4 kHz (Figure 3d). Beyond this frequency, the device response degrades due to insufficient carrier redistribution.

Spatial encoding capability was assessed using complementary "chessboard" patterns with values [1, 0] and [0, 1], subtracted to yield a [1, -1] pattern (Figure 3e). The SLM was mounted on a motorized stage for point-scanning across the x-y plane. Figure 3f shows the resulting differential pattern, indicating negligible crosstalk between adjacent pixels. Minor non-uniformities arise from variations in the n-GaAs layer or fabrication imperfections in the contacts. Three non-functional pixels (at (3,6), (7,1), and (9,5)) were excluded from subsequent imaging. Since compressive imaging using Hadamard patterns requires a power-of-two matrix dimension, an 8×8 subarray was selected from the upper-left region for further experiments.

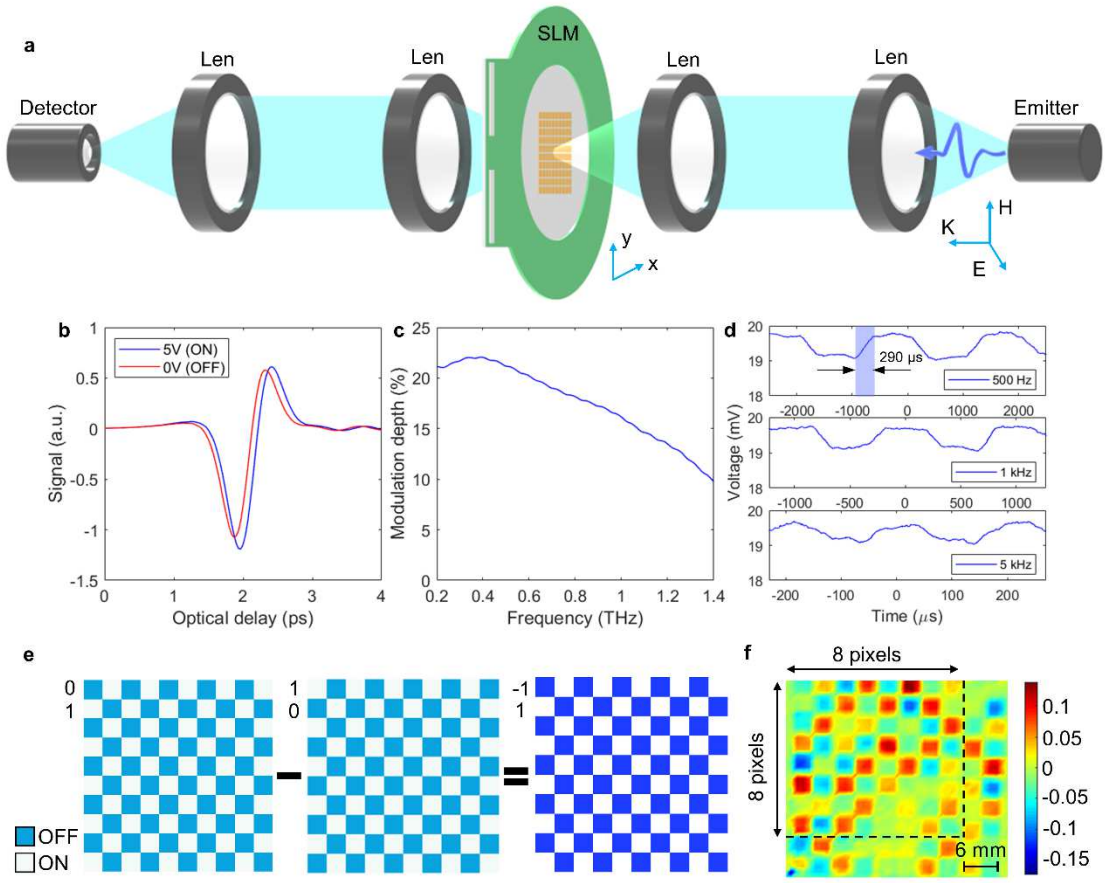


Figure 3. Characterization of spatial modulation performance of the SLM. a. Experimental configuration for raster-scanning the SLM using a focused terahertz beam. **b.** Time-domain signals of a representative pixel under 0 V (red curve) and 5 V reverse bias (blue curve). **c.** Frequency-dependent modulation depth calculated from the time-domain signals. **d.** Modulated terahertz signal amplitude measured at switching rates of 500 Hz, 1 kHz, and 5 kHz. **e.** Schematic illustration of projection pattern generation. Left: Initial pattern with 9 sign transitions per row and column, where "1" denotes 5 V bias and "0" denotes 0 V bias. Middle: Complementary pattern obtained by inverting the "1" and "0" assignments. Right: Differential signal between left and middle patterns, yielding a chessboard-like [1,-1] projection. **f.** Experimentally acquired chessboard pattern demonstrating spatial encoding capability of the SLM.

The "Diag" path terahertz single-pixel imaging algorithm

Single-pixel imaging enables image acquisition by interrogating a scene using a series of spatially controlled patterns, with the resulting integrated intensity captured by a single-element detector. After pixelation, the object can be mathematically represented as a column vector X with N elements. In the i-th measurement, the interrogation pattern is denoted by the row vector Φ_{ij}, which is multiplexed with the object. The detector collects the signal y_i, and after M measurements $(M \leq N)$, the process is formalized as the matrix equation $Y = \Phi X$, where $Y \in \mathbb{R}^{M\times 1}$, $\Phi \in \mathbb{R}^{M\times N}$, and $X \in \mathbb{R}^{N\times 1}$. When $M < N$, this inverse problem becomes ill-posed. Compressed sensing (CS) algorithms provide an efficient solution for image reconstruction by

leveraging sparse representations of signals [15]. Among various choices for the measurement matrix Φ, the Hadamard matrix is widely adopted due to its effectiveness in maximizing the signal-to-noise ratio (SNR) [16]. Furthermore, differential measurements using complementary Hadamard patterns enhance SNR by subtracting background noise and mitigating low-frequency oscillations from the illumination source [17,18]. The ordering of Hadamard patterns significantly influences reconstruction accuracy. Various sequencing strategies have been explored, including Natural [19], Walsh [19], Paley [20], Russian Doll (RD) [21], Cake-Cutting (CC) [22], Origami Pattern Construction (OPC) [23], and total variation-based ordering [24], each offering distinct advantages in specific contexts.

For natural images, low-frequency components typically exhibit higher energy in the sequency-ordered 2D Hadamard spectrum — a distribution consistent with frequency-domain characteristics observed in Fourier transforms [25]. The Hadamard spectrum, comprised of coefficients acquired via single-pixel detection, defines sequency as the number of sign changes in each basis pattern [26]. Thus, downsampling can be efficiently achieved by prioritizing the acquisition of low-sequency coefficients.

In this work, we developed a novel "Diag" sampling path for pattern ordering and employed the TVAL3 algorithm [27] for image reconstruction. The term "Diag" refers to the diagonal raster scanning sequence of the non-zero element in a two-dimensional Dirac-like pattern. As illustrated in Figure 4, this scanning strategy traverses along progressively lengthening diagonals, prioritizing the capture of high-energy coefficients before incorporating higher-sequency components. The corresponding Hadamard basis patterns are derived by applying the inverse Walsh – Hadamard transform to these Dirac-like patterns. In this transformation, the row index m and column index n correspond to the number of sign flips along the vertical and horizontal directions, respectively [28]. For instance, the pattern generated with a non-zero element at (2,2) (Figure 4a, upper left) results in exactly one sign flip along both directions.

The proposed Diag sampling path demonstrates significant advantages over conventional Hadamard orders (Natural[19], Walsh[19], Paley [20], and Cake-Cutting [22]) by achieving optimal energy compaction in low-sequency bands without requiring prior knowledge of the target. Whereas Natural order yields randomly distributed measurements that impair sampling efficiency, and Walsh/Paley orders only partially improve energy concentration, the Diag sequence ensures highly compact and efficient

measurement energy distribution. This inherent compaction provides an ideal foundation for accurate reconstruction in compressive sensing algorithms.

The Diag order is particularly advantageous under challenging imaging conditions, such as strong noise (10 dB SNR) and low sampling rates (20–40%). Its effectiveness stems from an energy-frontloaded acquisition sequence that captures high-SNR components early in the process, before noise contamination dominates in subsequent measurements. This design makes the Diag order exceptionally suitable for terahertz compressed sensing applications, where limitations in spatial light modulator modulation depth and post-interaction SNR often constrain performance. A detailed theoretical comparison is provided in Supplementary Information Figure S6.

Computational efficiency is critical for practical compressed sensing-based image reconstruction, as it enables real-time processing, handles high-dimensional data, and optimizes the trade-off between speed and accuracy. As shown in Table 1, comparative analysis between the Cake-Cutting (CC) and Diag methods reveals dramatic differences in scalability. While the CC method exhibits exponential runtime growth—from 0.001 s (for 16×16 matrices) to 84.2 s (for 4096×4096 matrices)—the Diag method maintains high efficiency, with runtime increasing only from 0.001 s to 0.47 s over the same range. At the 4096×4096 scale, the Diag method achieves a 99.4% reduction in runtime compared to CC, demonstrating superior scalability and practical utility for high-dimensional imaging applications. Our image reconstruction algorithm leverages the Diag method to capitalize on its enhanced noise robustness and computational efficiency.

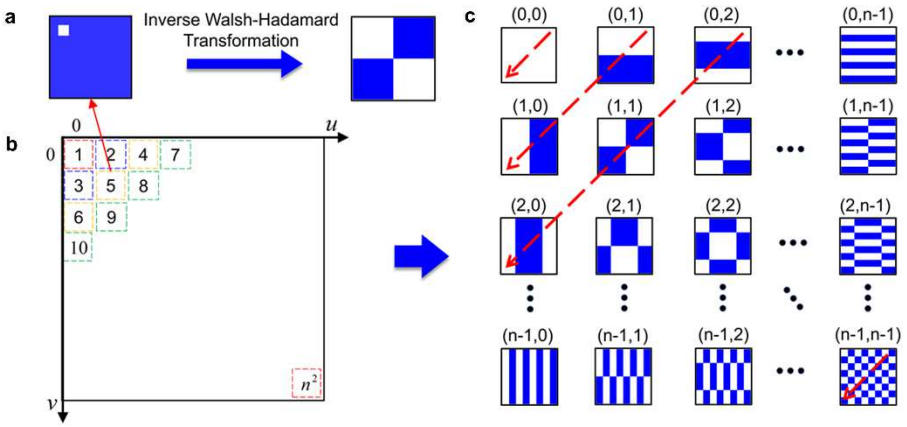


Figure 4. Illustration of diagonal ordering of Hadamard basis patterns from Dirac-like single-element patterns. a. Hadamard basis pattern generated by applying the inverse Walsh–Hadamard transform to a Dirac-like pattern with a single activated element at position (2,2) (upper left corner). White and blue squares represent values of +1 and -1, respectively. **b.**

Sampling sequence in the 2D frequency domain (u, v). Numbers indicate the order of selected Dirac-like patterns (single activated pixel), beginning at (u=0, v=0) (labeled 1). **c.** Hadamard basis patterns sampled in the sequence shown in **b**.

Table. Computational efficiency comparison between the Cake-Cutting (CC) and Diagonal (Diag) strategies for Hadamard pattern ordering.

Matrix size	CC strategy	Diag strategy
16×16	0.001 s	0.001 s
64×64	0.007 s	0.003 s
256×256	0.1 s	0.004 s
1024×1024	2.2 s	0.05 s
4096×4096	84.2 s	0.47 s

Note: The Diag strategy reduces runtime by over two orders of magnitude at the 4096×4096 scale, demonstrating superior scalability and efficiency for large-scale compressive imaging

The hyperspectral and three-dimensional terahertz single-pixel imaging

The experimental configuration for single-pixel imaging is illustrated in Figure 5a. Unlike the setup in Figure 3a, two plano-convex lenses were removed to generate a collimated terahertz beam. This collimated beam was spatially modulated using the SLM before transmission through the sample. An MCU controlled the SLM to project the prescribed Hadamard basis patterns. To enhance the SNR, differential measurements were acquired by displaying each Hadamard pattern followed by its complementary inverse pattern and computing the intensity difference. Figure 5b schematically depicts the sample—a metallic plate with a cross-shaped aperture having arm dimensions of 6 mm in both directions. Figure 5c displays the frequency-domain signal derived from the temporal data of the first pattern. To highlight the wideband imaging capability of the system, images were reconstructed at four distinct frequencies: 0.24 THz, 0.45 THz, 0.73 THz, and 1.12 THz, using a 70% sampling ratio (SR), where SR is defined as the number of measurements relative to the total number of image pixels (Fig. 5d–5g). Additional data on image quality evaluated by peak signal-to-noise-ratio at varying SRs are provided in Supplementary Fig. S7–S9. Employing a terahertz system with higher SNR in the future would enable the use of higher-order patterns for finer spatial detail.

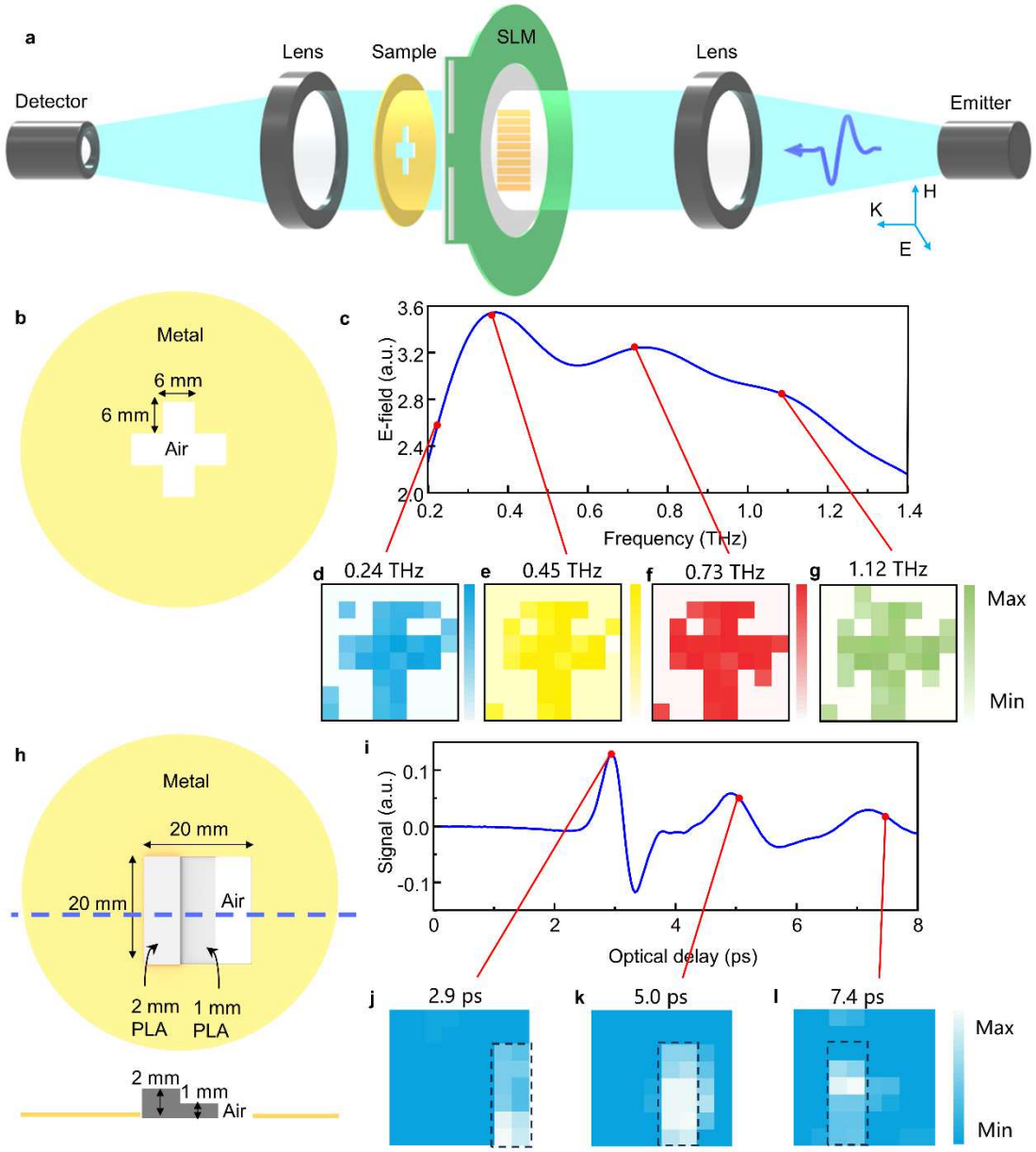


Figure 5. Experimental setup and applications of the ultrawideband spatial light modulator (SLM) for hyperspectral and 3D single-pixel imaging. a. Schematic of the single-pixel imaging system. A collimated terahertz beam is spatially encoded by the SLM and subsequently transmitted through the imaging object. **b.** Design of the imaging target: a metallic aperture in the shape of a cross, with both vertical and horizontal arms measuring 6 mm in length. **c.** Fourier-transform amplitude of the temporal signal corresponding to the first illumination pattern. **d-g.** Reconstructed images at selected frequencies of 0.24 THz, 0.45 THz, 0.73 THz, and 1.12 THz, acquired under a 70% sampling ratio (SR). **h.** Diagram of the multi-thickness 3D-printed object fabricated from polylactic acid (PLA). **i.** Measured terahertz waveform after propagation through the 3D-printed object, corresponding to the first pattern. **j-l.** Reconstructed images at distinct temporal slices of the terahertz waveform, illustrating depth-resolved imaging capability.

A significant advantage of the broad bandwidth is the capability for depth resolution, allowing reconstruction of 3D images through time-domain phase information. To demonstrate this, a multi-thickness polylactic acid (PLA) sample was fabricated (Fig. 5h), comprising a 2 mm thick section (left), a 1 mm section (middle),

and an open section (right). Temporal peaks at 2.9 ps, 5.0 ps, and 7.4 ps corresponded to transmissions through interfaces at different depths. By selecting time-delayed data, images were reconstructed for each interface (Fig. 5j–5l), confirming the 3D imaging capacity of the electrical SLM.

While transmission-mode imaging is effective for low-absorption materials, reflection-mode operation is essential for opaque samples, such as hydrated biological tissues. A normal-incidence reflection-mode setup is shown in Figure 6a. A metallic sample with variable thickness (inset, Fig. 6a) was imaged, with thick (2 mm) and thin (1 mm) regions each covering 20×20 mm^2, representing one-quarter of the total imaging area. The terahertz beam reflected from different sample interfaces was modulated by the SLM and detected. Ten patterns were used to capture corresponding temporal signals, with peak values employed for image reconstruction. Figure 6b shows the temporal signal of the first pattern, with reflections from two interfaces visible at 2.5 ps and 8.9 ps. Images reconstructed from time-delayed data at an 8% SR (Fig. 6c–6d) successfully resolved the two interfaces. The time difference of 6.4 ps corresponds to a 1.92 mm optical path difference in air, consistent with the physical step height of 1 mm in a double-pass geometry.

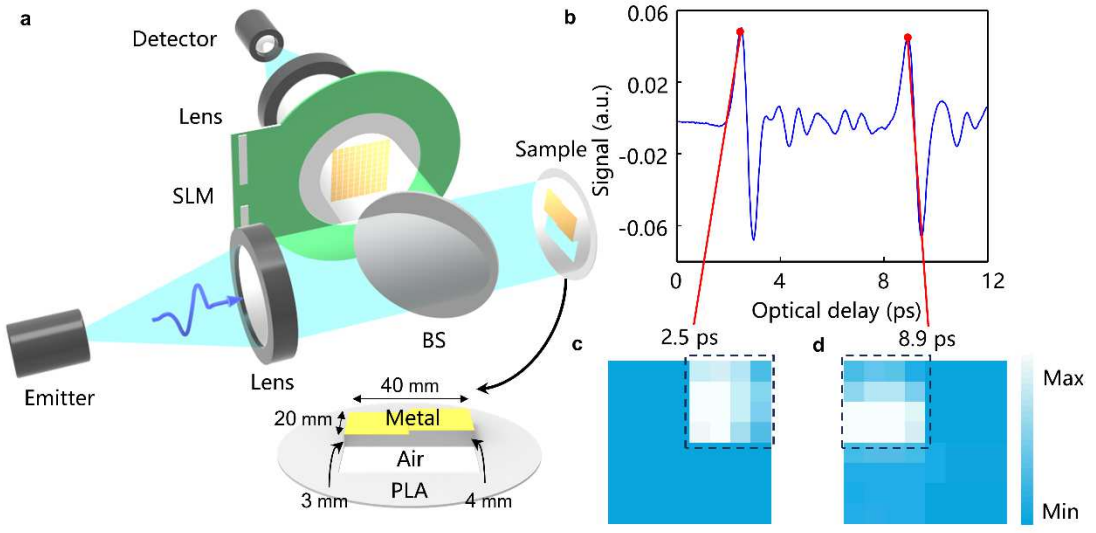


Figure 6. Normal-reflection single-pixel terahertz imaging system and interface-resolved reconstruction. a. Schematic of the reflection-mode imaging setup. BS denotes a high-resistivity silicon beam splitter. Inset: Imaging target comprising two regions with thicknesses of 3 mm and 4 mm, each occupying a 20×20 mm^2 area (quarter of the total area 40×40 mm^2 field). **b.** Time-domain reflected terahertz pulses showing distinct peaks corresponding to interfaces at 2.5 ps (thicker region) and 8.9 ps (thinner region). **c-d.** Reconstructed images from temporal slices at 2.5 ps and 8.9 ps, highlighting interface-specific resolution. Each sample region occupies one-quarter of the total imaging area.

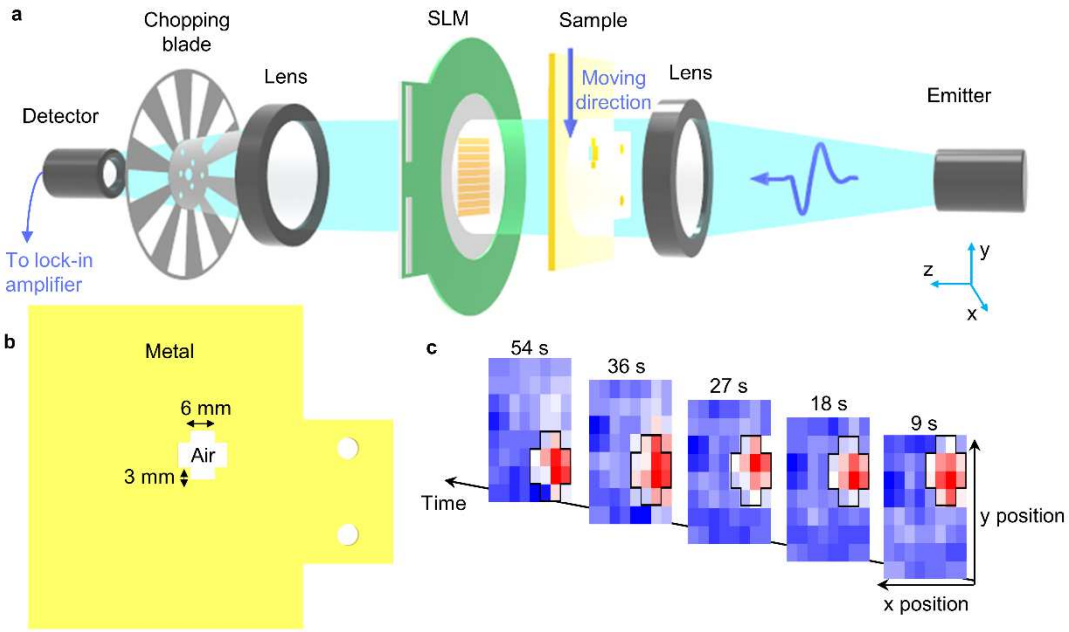


Figure 7. Schematic of the dynamic imaging experiment. a. Experimental setup for single-pixel dynamic imaging. A collimated terahertz beam is spatially modulated by the SLM before passing through a sample translating horizontally. A mechanical chopper placed upstream of the detector provides frequency modulation to enhance signal detection. **b.** Imaging target: a metallic plate with a cross-shaped aperture. **c.** Reconstructed terahertz images of the moving object, demonstrating a frame rate of 9 seconds per frame.

To evaluate the potential for real-time imaging, dynamic experiments were performed on a moving target. A mechanical chopper was introduced before the detector to provide stable carrier modulation, and a lock-in amplifier improved signal recovery. The imaging protocol involved sequentially displaying 60 masks with 80 ms per mask, achieving 46.8% data compression. After completing each set of patterns, the image was reconstructed using the Diag algorithm, and a translation stage moved the cross-shaped target horizontally. The system achieved a frame reconstruction time of 9 seconds. Figure 7c shows five consecutive frames (see Supplementary Movie 1), where the red cross (outlined in black) clearly translates against the background, successfully demonstrating motion tracking.

Discussion

The fidelity of image reconstruction in our system is fundamentally governed by the signal-to-noise ratio (SNR). As a first-generation prototype, the current electrical THz-SLM serves primarily as a proof-of-concept demonstration. To enhance image quality, several parameters of the modulator array can be optimized. These include tuning the free carrier density in the n-GaAs layer and refining the geometric dimensions (e.g., period and gap width) of the metal microslits. A promising strategy to

achieve deeper modulation depth involves depositing n-GaAs layers on both sides of the intrinsic GaAs substrate and fabricating dual SLM patterns, thereby enhancing light-matter interaction.

Spatial resolution can be further advanced by miniaturizing the pixel size via state-of-the-art fabrication techniques while maintaining the non-resonant microslit design. Furthermore, super-resolution imaging could be realized by positioning samples within the near-field region of the SLM and employing compressed sensing algorithms. Integration of emerging computational imaging techniques, such as pixel super-resolution (PSR) powered by convolutional neural networks (CNNs), also presents a promising avenue for surpassing the diffraction-limited resolution [7].

The imaging speed in the present study was primarily limited by the data acquisition electronics (PCB) and the THz-TDS setup, not by the intrinsic response of the GaAs-based SLM. Indeed, similar devices have demonstrated operational bandwidths exceeding 100 kHz [14] or even reaching the MHz regime with optimized design[29]. Replacing the pulsed TDS system with a continuous-wave (CW) terahertz source, coupled with an optimized high-speed control circuit, could drastically improve imaging throughput, potentially enabling real-time applications.

It is important to contextualize our system's performance against alternative approaches. Metamaterial-based SLMs, for instance, can achieve higher frame rates and possess a compact form factor by leveraging free-carrier-induced resonant frequency shifts. However, this strategy often sacrifices spectral bandwidth. In contrast, our hyperspectral SLM prioritizes ultrawideband performance and depth-resolution capabilities, trading off speed for enriched spectral and 3D imaging information. This distinction underscores a fundamental design choice tailored for spectroscopic and multidimensional applications rather than pure frame rate maximization.

In summary, we have developed a hyperspectral terahertz single-pixel imaging system enabled by an ultrawideband, electrically controlled SLM with a 100-pixel array. A novel "Diag" sampling strategy was introduced, which outperforms conventional Hadamard sequences by concentrating energy more efficiently in low-sequency regions without requiring a priori knowledge of the target. This approach facilitated successful hyperspectral image reconstruction across a broad range (0.2–1.4 THz) and enabled 3D imaging by leveraging time-domain terahertz pulses in both transmission and reflection modes. While the current frame acquisition time stands at approximately 9 seconds,

future enhancements—including higher-resolution modulator arrays, increased pixel counts, and improved SNR—are expected to significantly boost imaging quality. When integrated with a high-speed terahertz system, these improvements could pave the way for real-time imaging. Our system holds substantial promise for applications in non-destructive testing, security screening, biomedical diagnostics, and chemical identification, where spectroscopic signatures and depth resolution are paramount.

Materials and methods

Device fabrication and assembly

A 0.62 μm thick *n*-GaAs (dopant: Si) layer with a free carrier density of 2×10^{17} cm^{-3} (as measured by Accent ECVpro) was grown on via molecular beam epitaxy(MBE) on a 3-inch intrinsic GaAs substrate (supplied by AXT, Inc.). The "U"-shaped Ohmic contact was fabricated through electron beam deposition, sequentially depositing layers of 20 nm germanium, 20 nm gold, 20 nm nickel, and 200 nm gold, followed by rapid thermal annealing at 400 ℃ for 1 minute. Subsequently, the metal microslits and electrode lines were patterned using conventional photolithography. A 10-nm-thick titanium adhesion layer was first deposited onto the GaAs substrate via electron beam deposition, followed by a 200 nm gold layer, and completed with a lift-off process. Finally, the SLM was electrically integrated by connecting it to a printed circuit board through wire bonding.

Device characterization

Each pixel of the 10×10 pixel SLM was independently addressed by one of the 100 output channels (providing -5V or 0V) of a custom-built microcontroller unit (MCU). Chessboard patterns were loaded into the MCU to control the state of each pixel. The THz-SLM was mounted on a motorized positioning platform, which enabled raster scanning of the entire modulator surface with a focused teahertz beam.

Operating configurations

The experimental setup for terahertz single-pixel imaging incorporated the following components: a commercial terahertz time-domain spectroscopy (THz-TDS) system (TERA-K15, Menlo System Inc.); the custom-designed THz-SLM and its control units; a projection convex len (focal length f=100 mm); a collection convex len (f=100 mm); and a silicon beam splitter for reflection-type measurements.

Data processing

The intensity-based modulator exhibited binary transmission states, denoted as 1

(high transmission) and 0 (low transmission). To maintain the orthonormality inherent to Hadamard matrices (composed of elements +1 and -1), we performed sequential measurements for each pattern and its complementary inverse. Data were acquired from complementary pattern pairs with values [1, 0] and [0, 1]. For reconstructing an N-pixel image, a total of 2M (where $M \leqslant N$) full time-domain terahertz signals were recorded, corresponding to 2M distinct spatial encoding patterns.

To reconstruct images at specific temporal slices, data at selected time delays were extracted. The measurements for each pattern pair were then subtracted to obtain differential signals. The frequency-dependent amplitude of the terahertz signals was derived by applying a Fourier transform to the temporal data. For image reconstruction at specific frequencies, data at the desired frequencies were selected, and similarly, differential measurements were obtained by subtracting the complementary pattern pairs.

Acknowledgements

This work was supported in part by the National Natural Science Foundation of China [Grant Numbers U2330114, 62575188, T2421003, 62575187]; the Shenzhen Natural Science Foundation General Project [Grant Numbers JCYJ20230808105907015, JCYJ20240813141411015]; Special Projects in Key Areas of Guangdong Province [Grant Number 2022ZDZX2053]; the Natural Science Foundation of Guangdong Province [Grant Numbers 2019A1515010869, 2025A1515011392]; the Shenzhen University 2035 Plan Project; and the Shenzhen Key Laboratory of Photonics and Biophotonics [Grant Number ZDSYS20210623092006020].

Conflict of interest

The authors declare that they have no conflict of interest.

Data Availability Statement

The authors confirm that the data supporting the findings of this study are available within the article and its supplementary materials.

References

1 Lindley-Hatcher, H. *et al.* Real time THz imaging—opportunities and challenges for skin cancer detection. *Appl. Phys. Lett.* **118** (2021).

https://doi.org:10.1063/5.0055259
2 Patil, M. R., Ganorkar, S. B., Patil, A. S. & Shirkhedkar, A. A. Terahertz Spectroscopy: Encoding the Discovery, Instrumentation, and Applications toward Pharmaceutical Prospectives. *Crit. Rev. Anal. Chem.* **52**, 343-355 (2022). https://doi.org:10.1080/10408347.2020.1802219
3 Afsah-Hejri, L. *et al.* Terahertz spectroscopy and imaging: A review on agricultural applications. *Comput. Electron. Agric.* **177** (2020). https://doi.org:10.1016/j.compag.2020.105628
4 Cui, Y. *et al.* Hidden-information extraction from layered structures through terahertz imaging down to ultralow SNR. *Sci. Adv.* **9**, eadg8435-eadg8435 (2023). https://doi.org:10.1126/sciadv.adg8435
5 Knap, W. *et al.* Plasma wave detection of sub-terahertz and terahertz radiation by silicon field-effect transistors. *Appl. Phys. Lett.* **85**, 675-677 (2004). https://doi.org:10.1063/1.1775034
6 Nemoto, N. *et al.* High-Sensitivity and Broadband, Real-Time Terahertz Camera Incorporating a Micro-Bolometer Array With Resonant Cavity Structure. *IEEE Trans. Terahertz Sci. Technol.* **6**, 175-182 (2016). https://doi.org:10.1109/tthz.2015.2508010
7 Li, X. *et al.* Plasmonic photoconductive terahertz focal-plane array with pixel super-resolution. *Nature Photonics* **18**, 139-148 (2024). https://doi.org:10.1038/s41566-023-01346-2
8 Chan, W. L. *et al.* A single-pixel terahertz imaging system based on compressed sensing. *Applied Physics Letters* **93**, 121105 (2008).
9 Shen, H. *et al.* Spinning disk for compressive imaging. *Optics letters* **37**, 46-48 (2012).
10 Stantchev, R. I., Yu, X., Blu, T. & Pickwell-MacPherson, E. Real-time terahertz imaging with a single-pixel detector. *Nature Communications* **11**, 2535 (2020). https://doi.org:10.1038/s41467-020-16370-x
11 Chen, S.-C. *et al.* Terahertz wave near-field compressive imaging with a spatial resolution of over λ/100. *Optics Letters* **44**, 21-24 (2019). https://doi.org:10.1364/OL.44.000021
12 Novitsky, A. *et al.* Non-resonant terahertz field enhancement in periodically arranged nanoslits. *Journal of Applied Physics* **112**, 074318 (2012). https://doi.org:10.1063/1.4757024
13 Shi, S. *et al.* Optimizing Broadband Terahertz Modulation with Hybrid Graphene/Metasurface Structures. *Nano letters* **15**, 372-377 (2014).
14 Liu, X. *et al.* Ultrabroadband electrically controllable terahertz modulation based on GaAs Schottky diode structure. *APL Photonics* **6**, 111301 (2021). https://doi.org:10.1063/5.0064643
15 Burger, M., Foecke, J., Nickel, L., Jung, P. & Augustin, S. in *3rd International MATHEON Conference on Compressed Sensing and its Applications.* 263-290 (2019).
16 Watts, C. M. *et al.* Terahertz compressive imaging with metamaterial spatial light modulators. *Nature Photonics* **8**, 605-609 (2014). https://doi.org:10.1038/nphoton.2014.139 http://www.nature.com/nphoton/journal/v8/n8/abs/nphoton.2014.139.html#supplementary-information
17 Stantchev, R. I. *et al.* Noninvasive, near-field terahertz imaging of hidden objects using a single-pixel detector. *Sci. Adv.* **2** (2016). https://doi.org:10.1126/sciadv.1600190

18 Li, W. *et al.* Dual-color terahertz spatial light modulator for single-pixel imaging. *Light Sci Appl* **11**, 191 (2022). https://doi.org:10.1038/s41377-022-00879-5

19 Vaz, P. G., Amaral, D., Requicha Ferreira, L. F., Morgado, M. & Cardoso, J. Image quality of compressive single-pixel imaging using different Hadamard orderings. *Opt Express* **28**, 11666-11681 (2020). https://doi.org:10.1364/OE.387612

20 Stantchev, R. I., Yu, X., Blu, T. & Pickwell-MacPherson, E. Real-time terahertz imaging with a single-pixel detector. *Nat Commun* **11**, 2535 (2020). https://doi.org:10.1038/s41467-020-16370-x

21 Sun, M.-J., Meng, L.-T., Edgar, M. P., Padgett, M. J. & Radwell, N. A Russian Dolls ordering of the Hadamard basis for compressive single-pixel imaging. *Sci. Rep.* **7** (2017). https://doi.org:10.1038/s41598-017-03725-6

22 Yu, W. K. Super Sub-Nyquist Single-Pixel Imaging by Means of Cake-Cutting Hadamard Basis Sort. *Sensors (Basel)* **19** (2019). https://doi.org:10.3390/s19194122

23 Yu, W. K. & Liu, Y. M. Single-Pixel Imaging with Origami Pattern Construction. *Sensors (Basel)* **19** (2019). https://doi.org:10.3390/s19235135

24 Yu, X., Stantchev, R. I., Yang, F. & Pickwell-MacPherson, E. Super Sub-Nyquist Single-Pixel Imaging by Total Variation Ascending Ordering of the Hadamard Basis. *Sci Rep* **10**, 9338 (2020). https://doi.org:10.1038/s41598-020-66371-5

25 Radwell, N. *et al.* Single-pixel infrared and visible microscope. *Optica* **1** (2014). https://doi.org:10.1364/optica.1.000285

26 Pratt, W. K., Kane, J. & Andrews, H. C. HADAMARD TRANSFORM IMAGE CODING. *Proc. IEEE* **57**, 58-& (1969). https://doi.org:10.1109/proc.1969.6869

27 Li, C., Yin, W., Jiang, H. & Zhang, Y. An efficient augmented Lagrangian method with applications to total variation minimization. *Comput. Optim. Appl.* **56**, 507-530 (2013). https://doi.org:10.1007/s10589-013-9576-1

28 Geadah, Y. A. & Corinthios, M. J. G. NATURAL, DYADIC, AND SEQUENCY ORDER ALGORITHMS AND PROCESSORS FOR WALSH-HADAMARD TRANSFORM. *IEEE Trans. Comput.* **26**, 435-442 (1977).

29 Chen, H.-T. *et al.* Hybrid metamaterials enable fast electrical modulation of freely propagating terahertz waves. *Applied Physics Letters* **93**, 091117 (2008).

Supplementary Files

This is a list of supplementary files associated with this preprint. Click to download.

- SupplementaryInformation.docx